Effects of Surface Chemistry on the Mechanochemical Decomposition of Lubricant Additives

Egheosa Ogbomo,*[a,b,c] Fakhrul H. Bhuiyan,[d] Carlos Ayestarán Latorre,[a,b,c] Ashlie Martini,[d] and James P. Ewen*[a,b,c]

The growth of protective tribofilms from lubricant antiwear additives on rubbing surfaces is initiated by mechanochemical decomposition reactions. These processes are not well understood at the molecular scale for many important additives, such as tricresyl phosphate (TCP). One aspect that needs further clarification is the extent to which the surface properties affect the mechanochemical decomposition rate. In this study, we use nonequilibrium molecular dynamics (NEMD) simulations with a reactive force field (ReaxFF) to study the decomposition of TCP molecules confined and pressurised between sliding ferrous surfaces at a range of temperatures. We compare the decomposition of TCP on native iron, iron carbide, and iron oxide surfaces. We show that the decomposition rate of TCP molecules increases exponentially with temperature and shear stress, implying that this is a stress-augmented thermally activated process. The rates and products of decomposition depend on the properties of the confining surfaces. The activation energy, activation volume, and pre-exponential factor are similar for TCP decomposition between iron and iron carbide surfaces, but significantly different for iron oxide surfaces. These findings provide new insights into the mechanochemical decomposition of TCP and have important implications for the design of novel lubricant additives for use in high-temperature and high-pressure environments.

1 Introduction

Mechanochemistry describes a wide range of phenomena in which mechanical force influences chemical reactivity.[1] This includes reactions in ball mills, where energy is transferred from moving balls to the milled medium during collisions of the balls with each other and the jar walls.[2] Mechanochemical reactions can be performed without solvents or heating, which can provide considerable environmental benefits over conventional routes.[3] The choice of ball and jar materials are known to be affect reactivity for a range of processes, such as cocrystallisation[4] and cycloaddition,[5] emphasizing the important role of the solid material. In some cases, the milling balls themselves are the catalyst of the reaction, which is known at direct mechanocatalysis.[6] Another example and particularly high-value application of mechanochemistry is lubricant additives that reduce wear in tribological contacts.[7] The most popular antiwear additive for automotive lubricants, zinc dialkyldithiophosphate (ZDDP), forms protective tribofilms on rubbing surfaces through mechanochemical processes.[8–10]

The tribofilm growth of ZDDP is strongly dependent on the nature of the rubbing surfaces.[11] Surfaces with a high elastic modulus, such as tungsten carbide,[9] require lower loads to form tribofilms than steel, due to higher contact stresses.[10] In experiments using aluminium-silicon alloys, thicker ZDDP tribofilms form on the silicon phase than the aluminium matrix, which

is also due to the higher elastic modulus and thus stress.[12] As well as the mechanical properties of the rubbing surfaces, the surface energy can also affect ZDDP adsorption and tribofilm growth.[13] ZDDP forms thicker tribofilms on surfaces to which it readily adsorbs, such as steel, silicon nitride, and tungsten carbide surfaces than those where minimal adsorption occurs, such as diamond-like carbon (DLC) and silicon carbide.[14] Ion-implanting alloying elements into steel can affect ZDDP tribofilm growth, nickel promotes tribofilm formation, molybdenum and chromium slows growth, while vanadium and tungsten have no significant effect.[15] ZDDP forms thicker tribofilms on aluminium-magnesium alloys than on either of the pure metals due to the stronger adsorption of the ZDDP molecules on the alloy.[16] A recent study revealed how the interplay of mechanical and chemical factors determine the tribological behaviour of ZDDP on DLC, with hydrogen-free coatings of moderate elastic modulus being most wear-resistant while still allowing ultralow friction.[17] Surface chemistry can also affect other mechanochemical processes inside rubbing contacts. For example, the rate of α-pinene tribopolymerisation is higher on palladium, copper oxide, nickel oxide, and chromium oxide than gold, silicon oxide, aluminium oxide, and DLC surfaces.[18] Moreover, the α-pinene tribopolymerisation rate is higher on bare silica surfaces than hydroxylated silica.[19] This is due to the fact that stress can be more efficiently transferred from the sliding surfaces to additive molecules that are strongly adsorbed.[20,21]

Phosphate esters lubricant additives have numerous industrial applications due to their stability, particularly in the presence of oxygen.[22] Their versatility in structure, including the ability to incorporate a variety of substituent groups, has led to their application as lubricant additives to improve their antiwear, boundary lubrication, antioxidant, anti-corrosion, anti-foaming, and metal deactivation performance.[23] Phosphate esters come in various forms, including aromatic, alkyl, thiophosphates, and

[a] Department of Mechanical Engineering, Imperial College London, South Kensington Campus, SW7 2AZ London, U.K.;

E-mail: e.ogbomo21@imperial.ac.uk, j.ewen@imperial.ac.uk

[b] Institute of Molecular Science and Engineering, Imperial College London, South Kensington Campus, SW7 2AZ London, U.K.

[c] The Thomas Young Centre, Imperial College London, South Kensington Campus, SW7 2AZ London, U.K.

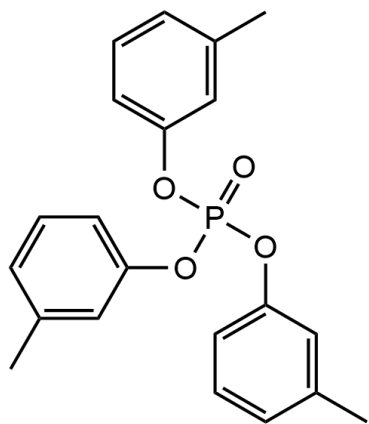[d] Department of Mechanical Engineering, University of California-Merced, 5200 N. Lake Road, Merced 95343 CA, U.S.A.

Fig. 1 Molecular structure of tri-meta-cresyl phosphate.

metal-containing esters, and are readily accessible for commercial use.[23] One of the most popular of these additives is tricresyl phosphate (TCP), which has been widely employed in aviation lubricants for gas turbine engines for decades.[24] The molecular structure of TCP is shown in Figure 1. Like ZDDP, TCP is an effective antiwear additive for steel contacts.[25,26] Another benefit of TCP for aviation lubricants is that the tribofilms it forms on metal surfaces slow the degradation of synthetic neopentyl polyol ester base stocks.[27]

It was initially suggested that the ability of TCP to reduce wear on steel surfaces originated from polishing of the surfaces through the formation of iron phosphide.[24] However, later studies showed that the major component of the tribofilms formed from TCP on steel was iron phosphate, which acted as a protective layer, rather than polishing the surfaces.[28–30] It has also been shown that either organic polyphosphates[31] or iron polyphosphates[32,33] are eventually formed from TCP inside tribological contacts, which are ultimately responsible for its antiwear performance on steel surfaces. At high temperatures, TCP molecules form relatively thick (60–100 nm) thermal films on steel surfaces;[34] however, aryl phosphates like TCP form thinner tribofilms ($\sim$ 20 nm) on rubbing surfaces.[35] This is much thinner that the ZDDP tribofilms that form on rubbing steel surfaces ($\sim$ 100 nm).[36]

The thermal decomposition of TCP has been studied on several different substrates. Wheeler and Faut[37] used X-ray photoelectron spectroscopy (XPS) to compare the adsorption and dissociation of TCP on gold and iron surfaces. On both substrates, adsorption saturated at about one monolayer, but adsorption was slower on gold than on iron.[37] TCP underwent non-dissociative adsorption on gold and desorbed upon heating, with no TCP left on the surface at 473 K.[37] On iron, no desorption occurred upon heating and additional interactions were observed between the substrate and the tolyl groups on the TCP molecule.[37] TCP decomposed on iron between 423 K and 473 K with one of the tolyl groups being removed to form iron phosphate.[37] The temperature range for decomposition is close to the temperature at which TCP significantly reduced the friction of rubbing steel surfaces in tribometer experiments.[30] It has since been shown that decomposition of TCP on iron surfaces occurs mainly via P-O bond scission to form methylphenoxy intermediates.[38] When TCP was heated to

800 K on iron, the methylphenoxy intermediates either desorbed as cresol via hydrogenation or decomposed further to generate tolyl intermediates.[38] Some of these tolyl intermediates desorbed as toluene via hydrogenation, but the majority decomposed resulting in hydrogen and carbon monoxide desorption and carbon deposition onto the iron surface.[38]

The steel surfaces inside tribological contacts are chemically heterogeneous and comprise multiple iron oxides.[39,40] From experiments conducted at high temperature (750 K), it was suggested that, due to acid-base reactions, TCP vapor preferentially reacts with iron in higher oxidation states, with reactivity increasing in the order: Fe $<$ FeO $<$ Fe$_3$O$_4$ $<$ Fe$_2$O$_3$.[32] However, more recent experiments suggested that reactivity towards TCP increases in the order Fe$_3$O$_4$ $<$ Fe $<$ Fe$_2$O$_3$.[41] In both of these experimental studies, the Fe surfaces will also form oxide layers that react with the TCP, rather than the native metal.[41] In addition to surface oxides, metal carbides are another important component of bearing steels.[42] A previous study of thermal decomposition found that TCP reactivity increases in the order: tungsten carbide $<$ molybdenum carbide $<$ chromium carbide $<$ vanadium carbide.[43]

In recent years, experimental studies of TCP adsorption and decomposition have been complemented by molecular simulations. For example, Khajeh et al.[45] used molecular dynamics (MD) simulations with a reactive force field (ReaxFF) to study the adsorption of TCP on hydroxylated amorphous Fe$_3$O$_4$. They found that, at lower temperatures ($\leq$ 500 K), chemisorption occurred mostly via Fe-C bond formation through the tolyl groups. At higher temperatures (600-700 K), a significant amount of Fe-O and O-P bonding also occurred, indicating chemisorption through the central phosphate group. Ewen et al.[46] compared the chemisorption and dissociation of TCP to trialkyl phosphates on Fe$_3$O$_4$(001) surfaces. In agreement with previous experiments,[38,47] they found that the triaryl phosphate TCP was much less reactive compared to the trialkyl phosphates. The MD simulations also showed that, while the main decomposition mechanism for trialkyl phosphates was C-O bond dissociation, the only bonds that broke in TCP were P-O bonds.[46] For the trialkyl phosphates, Ewen et al.[46] also compared the adsorption and dissociation on Fe$_3$O$_4$(001) to hydroxylated amorphous Fe$_3$O$_4$ and α-Fe surfaces. They found that the reactivity of the trialkyl phosphates increased in the order: hydroxylated amorphous Fe$_3$O$_4$ $<$ Fe$_3$O$_4$(001) $<$ α-Fe. Ayestarán Latorre et al.[48] studied the mechanochemical decomposition of trialkyl phosphates between sliding iron surfaces using non-equilibrium molecular dynamics (NEMD) simulations with ReaxFF. They found that secondary trialkyl phosphates were much more reactive than primary ones,[48] in agreement with previous experiments on ZDDP.[10] The influence of surface chemistry on the mechanochemical response of organophosphates is yet to be explored either experimentally or through NEMD simulations.

In this study, we use NEMD simulations with ReaxFF to compare the mechanochemical decomposition of TCP molecules confined between different ferrous surfaces over a range of temperatures and pressures. We observe significant differences in the mechanochemical reactivity of TCP on iron, iron oxide, and iron carbide surfaces. The variations in reactivity can be explained by differences in surface energy and stiffness, which can be ac-
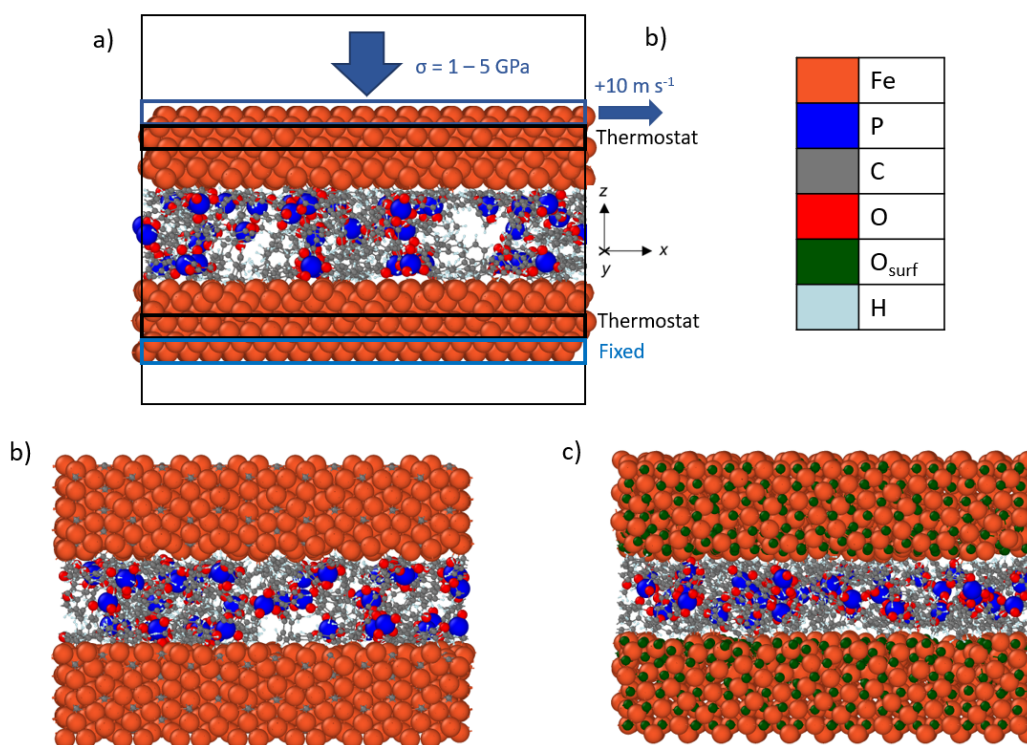
Fig. 2 Side-view snapshots showing the model systems with TCP molecules confined between a) α-Fe(110), b) Fe$_3$C(010), and c) Fe$_3$O$_4$(001)-SCV surfaces. Systems shown after minimisation and equilibration, but before heating, compression, and shear. Rendered using OVITO. [44]

counted for in theoretical models for mechanochemistry.

2 Methodology

We used NEMD simulations [49] to compare the mechanochemical reactivity of TCP on three ferrous surfaces, as shown in Figure 2. TCP is a molecule composed of three cresyl (methylphenyl) groups linked to a phosphate group. It is produced from cresol, which naturally contains a mixture of isomers with the methyl group in the ortho-, meta- and para-positions. The ortho-isomers of TCP are known to be toxic and modern production methods have reduced the concentration of these to very low levels. [50] Therefore, the TCPs used in current aviation lubricants generally contain mixtures of the meta-isomers and also some para-isomers. [50] The para-isomers were shown to have poorer lubricating properties compared to mixtures of isomers. [29] However, a recent study showed that the para-isomer is only slightly more reactive than the meta-isomer on ferrous surfaces. [41] In this study, we chose to study pure tri-meta-cresyl phosphate for simplicity; its molecular structure is shown in Figure 1.

All the systems were constructed using the Materials and Processes Simulations (MAPS) platform from Scienomics SARL. The three model surfaces were native iron, cementite, and magnetite. Symmetrical contacts were used with the same material for the upper and lower surface. Native iron surfaces were considered due to the possibility that they are exposed to the additive following removal of surface oxides in rubbing steel contacts. [51] Cementite was chosen as a representative iron carbide surface because it was identified in previous thermal degradation experiments using

TCP. [52] Magnetite was selected since previous experiments have shown that it is the major oxide formed on the surface of bearing steel following tribometer experiments. [39] We used an α-Fe(110) for the iron surface, [53] Fe$_3$C(010) as the cementite surface, [54] and Fe$_3$O$_4$(001) with a subsurface cation vacancy (SCV) reconstruction as the magnetite surface [55] due to their relatively low surface energies.

Periodic boundary conditions were applied in the x and y directions. Since the materials all had different lattice constants, it was not possible to create periodic surfaces with exactly the same dimensions. The α-Fe(110) surfaces had dimensions of $x = 4.8$, $y = 4.8$ and $z = 1.1$ nm. The Fe$_3$C(010) surfaces had dimensions of $x = 4.9$, $y = 4.7$ and $z = 1.05$ nm. The Fe$_3$O$_4$(001) surfaces had dimensions of $x = 5.0$, $y = 5.0$ and $z = 1.1$ nm. At the start of the simulations, two of each type of surface were separated by a 3.0 nm in the z-direction.

48 TCP molecules were inserted between the surfaces. No base oil molecules were present in the current simulations. Previous NEMD simulations showed that there were only minor differences when non-reactive base oils were included in the simulations. [56] To replicate tribometer experiments under full-film EHL conditions, [9,10,57] we ensured that no direct contact between the sliding ferrous surfaces occurred during the simulations.

All the simulations were performed using the Large-scale Atomic/Molecular Massively Parallel Simulator (LAMMPS) open-source software. [58] The velocity Verlet [59] integration scheme was used with a timestep of 0.25 fs. [45] The simulations were conducted in three phases: energy minimisation, equilibration, and
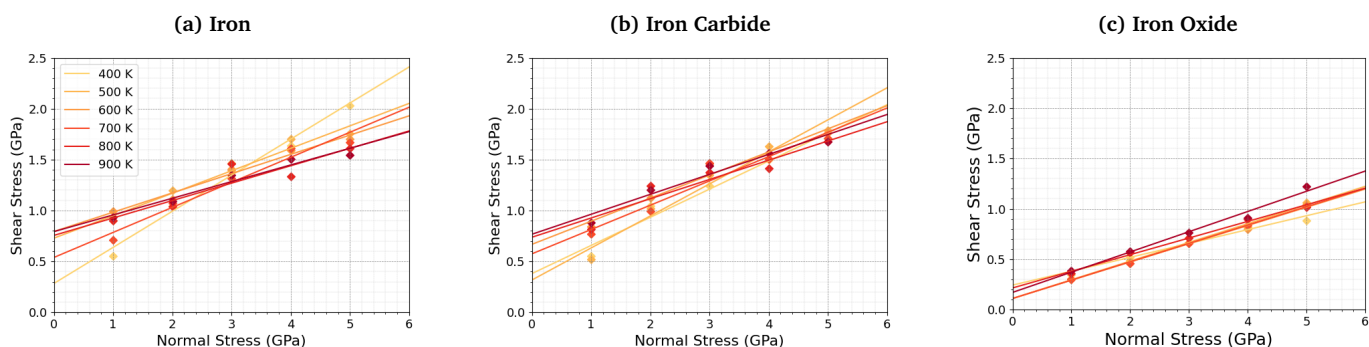
Fig. 3 Variation in shear stress with changes in normal stress for a) α-Fe(110), b) Fe$_3$C(010), and c) Fe$_3$O$_4$(001) surfaces.

then simultaneous heating, compression, and shear. The energy minimisation phase was conducted using the conjugate gradient method. For all the systems and conditions investigated, equilibration was performed at an ambient temperature of 300 K for 0.1 ns. During the equilibration phase, the two ferrous surfaces were brought closer together by applying a pressure of 10 MPa. The target pressure was obtained by applying a constant normal force equally distributed across the topmost layer of atoms in the upper surface, as shown in Figure 2a. The lowermost layer of atoms in the bottom surface was kept fixed in the z-direction. This ensured that a realistic liquid density of TCP (1.2 ± 0.1 g cm^{-3}) was obtained prior to the heating, compression, and shear phase. After the equilibration phase, the compression and shear phase of the simulations were run for 1 ns. Here, a constant sliding speed of 10 m s^{-1} was applied to the outer layer of atoms in the upper surface, as shown in Figure 2a. The pressure was increased to the target value of 1-5 GPa. The temperatures were increased to 400-900 K using a Langevin thermostat with a damping parameter of 25 fs.[60] The thermostat acted only in the y-direction and on the central layer of atoms in the upper and lower surfaces, as shown in Figure 2a. This approach enabled a temperature gradient to develop in the centre of the TCP film and heat to be dissipated at the surfaces, as would occur experimentally.[61] The thermostat was sufficiently efficient to ensure that the average system temperature was within 10 K of the target value at the applied sliding velocity.

The temperature, pressure, and sliding velocity were all increased simultaneously to capture their combined effects on the reaction rate. Some previous NEMD simulations of mechanochemical reactions with ReaxFF have isolated the effects of temperature, pressure, and sliding by using separate phases of the simulations.[20,62,63] The number of additive molecules in the NEMD simulations is finite, so separating the simulations into different phases (e.g. temperature) means that fewer molecules are available to react in any subsequent phases (e.g. sliding). Conversely, in experimental mechanochemistry studies,[9,10,57] additive-containing lubricants are continuously entrained between the sliding surfaces, effectively providing an infinite number of additive molecules. Hence, in our NEMD simulations, we elected to increase the temperature, pressure, and sliding velocity to their target values concurrently.[48]

Chemical bonding information was output every 1.0 ps, using a bond order cutoff of 0.3 to identify covalent bonds.[45] The choice of bond order cutoff only affects the post-processing analysis and does not influence the ReaxFF energy or force calculations during then NEMD simulations.

We used the bond order-based ReaxFF potential for all of the NEMD simulations. Similar systems consisting of phosphorus-containing additives confined between iron surfaces have previously been studied with NEMD simulations using first principles methods.[64,65] However, bond order potentials are several orders of magnitude cheaper than first principles methods,[66] allowing much larger systems to be simulated under experimentally-relevant conditions. ReaxFF was originally developed by van Duin et al.[67] to study hydrocarbon reactivity and has been parameterised to model a wide range of chemical systems and processes.[68] Of particular relevance to this study, ReaxFF-based NEMD simulations are now routinely used to study tribochemical reactions.[69]

The C/H/O/Fe/P ReaxFF parameters used in this study were developed by Khajeh et al.[45] The point charges on the atoms vary dynamically during the simulations and were calculated using the charge equilibration (QEq) method.[70] The parameters for Fe/O/H were originally developed by Aryanpour et. al.[71], Fe/C by Zou et. al.[72], P/O/C/H by Verlackt et. al.[73], and C/H/O by Chenoweth et. al.[74]. The combined C/H/O/Fe/P ReaxFF parameters[45] have been successfully applied to study the thermal and mechanochemical decomposition of phosphate esters with different alkyl and aryl substituents on several ferrous surfaces.[41,46,48] The ReaxFF parameters have also been validated against first principles calculations for the adsorption energy and dissociation energy for trialkyl phosphates on α-Fe(110).[46] The ReaxFF parameters for Fe/O/H have been shown to accurately reproduce the experimental lattice constants for α-Fe (within 1 %),[72] Fe$_3$C (within 0.5 %),[72] and Fe$_3$O$_4$ (within 3 %).[71] The ReaxFF parameters have also been shown to perform favourably compared to other many-body force fields in describing the mechanical properties of α-Fe.[75] At 300 K, the experimental elastic modulus is 166 GPa for α-Fe,[76] 174 GPa for Fe$_3$C,[77] and 186 GPa for Fe$_3$O$_4$(100).[78] With the ReaxFF parameters used here,[45,71,72] the bulk elastic modulus at 300 K is 136 GPa for α-Fe,[79] 148 GPa for Fe$_3$C,[79] and 129 GPa for Fe$_3$O$_4$.[80] Thus, at 300 K, the experi-

mental bulk elastic modulus is underpredicted by 18 % for α-Fe, 15 % for Fe$_3$C, and 31 % for Fe$_3$O$_4$. Since previous density functional theory (DFT) calculations have highlighted the importance of contact stiffness to mechanochemical processes,[81] we also calculated the elastic properties of thin single slabs of the three materials used in the NEMD simulations. For this calculation, the lowermost layer of atoms in each slab of material was fixed in the z-direction, while a constant normal force was applied the topmost layer of atoms to compress the system to 2 GPa. The temperature was varied between 300-900 K using the same thermostat as applied in the NEMD simulations. The corresponding elastic constant (C_{33}) was calculated from the strain fluctuations at constant normal stress.[82] The elastic constant results for the thin slabs are shown in the Electronic Supplementary Information (ESI) (Table S1). For the α-Fe(110) slabs, the elastic constant C_{33} decreases from 206 GPa at 300 K to 196 GPa at 900 K. The elastic constant C_{33} also decreases with increasing temperature for the Fe$_3$C(010) (from 200 GPa to 181 GPa) and Fe$_3$O$_4$(001) (from 220 GPa to 196 GPa) slabs. The higher stiffness of thin solid slabs compared to bulk solids was also observed in previous MD simulations and was attributed to geometrical confinement.[83] The decreasing stiffness with increasing temperature is also consistent with previous experiments.[76]

3 Results and Discussion

3.1 Shear Stress

Previous studies have shown that the tribofilm growth rate of antiwear additives is dependent on the shear stress as opposed to the normal stress.[9,10] It is therefore important to understand the relationship between the normal stress and shear stress in our systems. The steady-state shear stress was block averaged over the final 0.5 ns of the NEMD simulations. Figure 3 shows the relationship between applied normal stress and the measured shear stress for the three ferrous surfaces. At any temperature and normal stress, the shear stress is lower for the systems with TCP molecules sheared between iron oxide surfaces than iron and iron carbide surfaces. For all three surfaces, the shear stress increases linearly with normal stress with a finite intercept, as predicted by the extended Amontons-Coulomb law: $\tau = \mu\sigma + \tau_0$, where τ is the shear stress, μ is the friction coefficient, τ_0 is the Derjaguin offset, and σ is the normal stress.[84] The friction coefficient and Derjaguin offset for the different systems and temperatures are shown in the ESI (Tables S2 and S3). The friction coefficient, given by the gradient of the linear fits in Figure 3, is similar for all three surfaces. The Derjaguin offset, given by the intercept of the linear fit, is similar for iron and iron carbide surfaces, but is around 50 % lower for iron oxide. This is likely due to the higher surface energy and adhesion of TCP molecules on iron and iron carbide compared to iron oxide.[13] Previous DFT calculations suggested that the surface energy of α-Fe(110) (2.3 J m^{-2})[53] and Fe$_3$C(010) (2.2 J m^{-2})[54] is much larger than Fe$_3$O$_4$(001) (1.0 J m^{-2}).[85] For the iron and iron carbide systems, the friction coefficient decreases with increasing temperature (Table S2); in contrast, the Derjaguin offset increases with increasing temperature (Table S3). As the temperature increases, the amount of TCP de-

composition will also increase,[46] which causes the temperature-dependence of the friction coefficient and Derjaguin offset. For the iron oxide surfaces, the temperature has a negligible effect on the friction coefficient and Derjaguin offset, which is probably due to the lower reactivity of TCP on this surface.[46]

3.2 Dissociation Rates of TCP on Ferrous Surfaces

Figure 4 shows the change in the number of intact TCP molecules with time for α-Fe(110), Fe$_3$C(010), and Fe$_3$O$_4$(001) surfaces at constant normal stress (4 GPa) and varied temperature (400-900 K), and constant temperature (600 K) and varied normal stress (1-5 GPa). The reduction in the number of intact TCP molecules with time is shown for several other conditions in the ESI (Figure S1). The TCP molecules are counted as dissociated, i.e., no longer intact, if any bond other than C-H is broken. During the NEMD simulations, there is an exponential decay in the number of intact TCP molecules with time, which is indicative of a first-order reaction.[86] This observation is in agreement with previous NEMD simulations of trialkyl phosphate decomposition between α-Fe(110) surfaces.[48] In mechanochemistry experiments with ZDDP, the rate of tribofilm growth followed either zero-order or fractional-order kinetics.[8,10,57] The observation of zero-order kinetics indicates that the rate-determining step for tribofilm growth involves surface-adsorbed molecules, which masks the underlying first-order kinetics.[87] In experiments, the surface-adsorbed additive molecules are continually replenished from the base oil solution and the bulk concentration does not significantly decrease.[10] On the other hand, there is a finite number of additive molecules in the NEMD simulations, which means that the dissociation rate inevitably decreases as fewer molecules are available to react.[48] The dashed lines in Figure 10 show the simulation data and the solid lines are fits to an exponential function. The exponential decay curves are used to calculate the decomposition rate for each temperature and stress condition. The full tables of the TCP decomposition rates obtained from the 2D fits for all the conditions and surfaces can be found in the ESI (Tables S4, S5, and S6).

The study by Ayestarán Latorre et. al.[48] investigated the mechanochemical decomposition of trialkyl phosphates between 300-500 K and 1-4 GPa for α-Fe(110) surfaces. Comparing the current results to this previous study, it is clear that triaryl phosphates such as TCP had much lower decomposition rates than trialkyl phosphates under the same conditions. This observation agrees with previous experimental[38,47] and simulation[46] studies of the thermal decomposition of phosphate esters on ferrous surfaces.

3.3 Effects of Surface Chemistry on Bonding Rates

The TCP decomposition rates vary significantly depending on the surface chemistry, with the fastest dissociation being observed for the α-Fe(110) systems, followed by Fe$_3$C(010), and finally Fe$_3$O$_4$(100). This may be due to the differences in surface energies of the three ferrous surfaces.[53,54,85] Higher surface energies promote stronger molecular adsorption[88] and thus faster TCP decomposition. DFT calculations have shown that adsorption is a crucial step the decomposition of TCP on iron surfaces.[89] Disso-
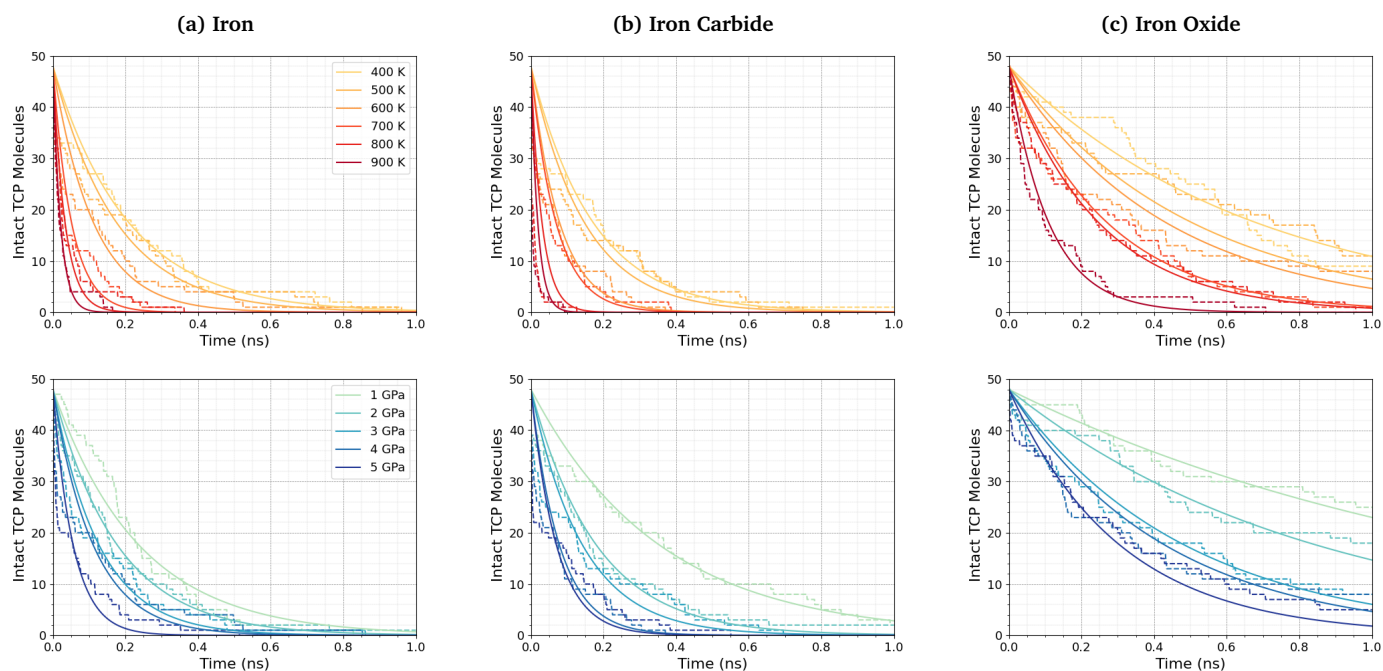
Fig. 4 Change in the number of intact TCP molecules with time at 4 GPa between 400-900 K and at 600 K between 1-5 GPa for a) α-Fe(110), b) Fe$_3$C(010), and c) Fe$_3$O$_4$(001) surfaces. The dashed lines show the simulation data and the solid lines are exponential decay fits to these data.

ciative chemisorption is the rate-determining step for many heterogeneously catalysed processes.[90]

Previous experimental thermal decomposition studies showed that TCP preferentially reacted with iron oxides that were in a higher oxidation state, i.e. Fe < FeO < Fe$_3$O$_4$ < Fe$_2$O$_3$.[32] This contrasts with first principles NEMD simulations of other lubricant additives, such as molybdenum dithiocarbamates, where native iron surfaces were found to be much more reactive than oxidised surfaces.[91] In agreement with the simulations by Peeters et al.[91], we observe much higher mechanochemical reactivity on the iron surface compared to the iron oxide surface.

Previous MD simulations investigating the thermal decomposition of TCP on hydroxylated amorphous Fe$_3$O$_4$ showed that the dominant reaction pathway involved Fe-C bonding.[45] To investigate this further, we plotted the change in the number of carbon atoms bonded to iron atoms at different pressures and temperatures. The Fe-C bonds present in the Fe$_3$C(010) surfaces before exposure to TCP are not included in the analysis. Figure 5 shows the variation in the number of Fe-C bonds with time for the simulated TCP systems at 600 K between 1-5 GPa for α-Fe(110), Fe$_3$C(010), and Fe$_3$O$_4$(100). The number of Fe-C bonds at a given time increases as Fe$_3$O$_4$(100) < Fe$_3$C(010) < α-Fe(110), which is the same order observed for the rates of TCP decomposition for the three surfaces. We also see a clear trend of an increase in the number of Fe-C bonds, and therefore chemisorption of TCP, with an increase in pressure for all three surfaces. The increased bonding of the TCP carbon atoms on α-Fe(110) compared to Fe$_3$C(010) and Fe$_3$O$_4$(100) can be visualised in the number density profiles shown in the ESI (Figure S2). The carbon peaks from the TCP molecules show increased overlap with

the iron peaks for α-Fe(110) than the other surfaces.

Figure 6 shows the relationship between the number of Fe-C bonds formed and the TCP decomposition rate. There is a logarithmic increase in the TCP decomposition rate with the number of Fe-C bonds formed for all three surfaces. This implies that increased chemisorption of the molecules leads to faster dissociation.[13] Indeed, previous experiments showed that ZDDP forms thicker tribofilms on surfaces to which it more strongly adsorbs.[14]

3.4 TCP Decomposition Mechanisms

Figure 7 shows the change in the total number of C-O and P-O bonds with sliding time for an intermediate temperature (500 K) and pressure (3 GPa). For the Fe$_3$O$_4$(001) surfaces, bonds with surface oxygen atoms are included in the analysis. Solid lines represent the total change in the number of bonds compared to the TCP molecules, dotted lines show the contribution from bonds in TCP that are broken, and dashed lines show new bonds that are formed. For all the surfaces, approximately five times as many P-O bonds are broken than C-O bonds, suggesting that P-O cleavage dominates over C-O cleavage. This is expected based on previous MD simulations[41,46] and experiments[38] of the thermal decomposition of TCP for triaryl phosphates. Conversely, in previous NEMD simulations of trialkyl phosphates confined between α-Fe(110) surfaces, approximately twice as many C-O bonds were broken than P-O bonds.[48] The decomposition mechanism is therefore affected by the much stronger C-O bonds in triaryl phosphates relative to those in trialkyl phosphates. Moreover, unlike triaryl phosphates, some alkyl intermediates formed by C-O cleavage in trialkyl phosphates, such as butyl chains, can readily undergo β-hydride elimination reactions on ferrous sur-
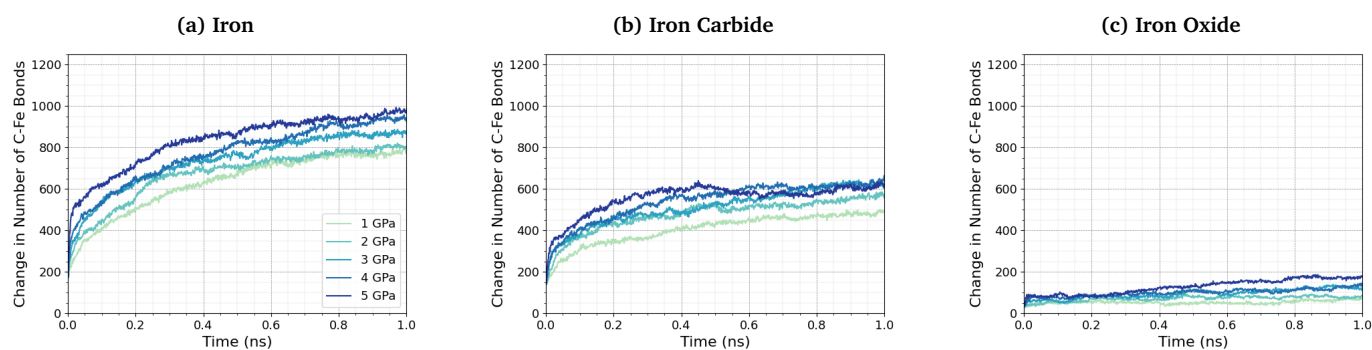
Fig. 5 Number of Fe-C bonds as a function of time at 600 K between 1-5 GPa for a) α-Fe(110), b) Fe$_3$C(010), and c) Fe$_3$O$_4$(100).

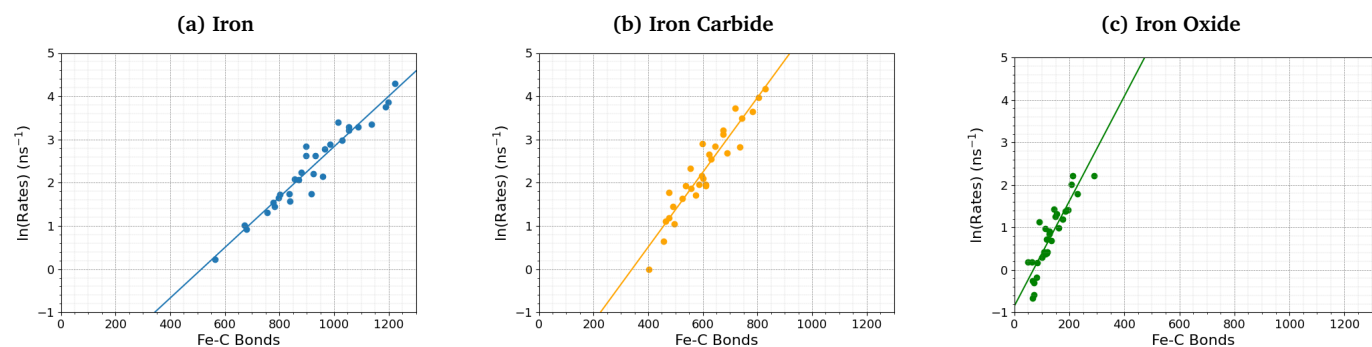
Fig. 6 Variation in the TCP decomposition rates with change in the number of Fe-C bonds between 0-1 ns for a) α-Fe(110), b) Fe$_3$C(010), and c) Fe$_3$O$_4$(100).

faces to produce gaseous olefins.[38] In Figure 7, the number of C-O and P-O bonds broken for the α-Fe(110) and Fe$_3$C(010) surfaces is similar, but fewer bonds are broken for the Fe$_3$O$_4$(001) surfaces.

No direct Fe-P bonds formed between the surfaces and TCP molecules in any of the NEMD simulations, which indicates that iron phosphate, rather than iron phosphide, is formed on the ferrous surfaces, consistent with observations in previous studies.[28–30] More P-O bonds are formed than are broken in the TCP molecules, leading to an overall increase in the number of P-O bonds, as shown by the solid blue lines in Figure 7. This is due to the formation of P-O-P linkages between the phosphorus atoms, leading to polyphosphate growth.[32,33] This process occurs mainly through nucleophilic substitution reactions, whereby P-O-R bonds in TCP (where R is a cresyl group) are replaced by P-O-P bonds.[48]

The total increase in the number of P-O bonds at the end of the 1 ns simulation is similar (40-50 bonds) for the α-Fe(110), Fe$_3$C(010), and Fe$_3$O$_4$(001) surfaces. This is because both the P-O cleavage and P-O formation reactions are accelerated by the more reactive surfaces (α-Fe(110)), as shown by the steeper dashed blue lines in Figure 7. The total number of P-O bonds at the end of the simulation is also not sensitive to the temperature and pressure, as shown in the ESI (Figure S3).[48]

For the Fe$_3$O$_4$(001) surface, nucleophilic attack from the surface oxygen atoms could increase the rate of P-O dissociation in the TCP molecules.[46] The variation in the number of P-O$_{surf}$ bonds formed between phosphorus atoms in the TCP molecules

and oxygen atoms in the Fe$_3$O$_4$(001) surface is shown in the ESI (Figure S4). At low temperature and pressure, the number of P-O$_{surf}$ bonds formed (Figure S4) is much less than the total number of P-O bonds formed (Figure 7), suggesting that this process plays a negligible role in nucleophilic substitution reactions. However, at high temperature and pressure, the number of P-O$_{surf}$ bonds increases, such that it they represent a significant proportion (>10 %) of the total P-O bonds formed.

3.5 Effects of Surface Chemistry on Tribofilm Growth

Figure 8 shows the number of phosphate-containing oligomers, toluene, and cresol molecules formed from TCP at 500 K and 3 GPa on the three surfaces. On iron and iron carbide, the primary product of TCP decomposition is cresol, formed by P-O bond cleavage. Some toluene is also formed on these surfaces via C-O cleavage, but this occurs only after the formation of cresol. The number of oligomers formed is similar for all three surfaces. However, on iron oxide, phosphate-containing oligomers are the major product.

The length of the polyphosphate chains in tribofilms is important to their antiwear performance.[92] Figure 9 shows the change in the number of polyphosphate chains (dimers, trimers, tetramers, and $\geq$ pentamers) with sliding time for the three studied systems. In all cases, the total number of polyphosphate fragments increases at short times before asymptoting towards a steady-state value of $\sim$10. For Fe$_3$C(010) and Fe$_3$O$_4$(001), the majority of TCP molecules form dimers, but longer chains, up to
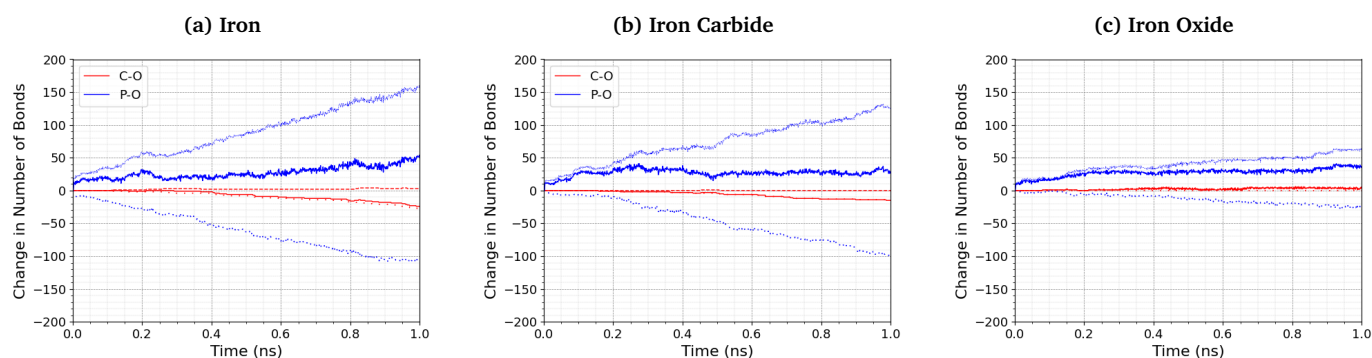
Fig. 7 Change in the number of P-O and C-O bonds with sliding time at 500 K and 3 GPa for the a) α-Fe(110), b) Fe$_3$C(010), and c) Fe$_3$O$_4$(001) systems. Solid lines show the change in the total number of bonds compared to TCP, dashed lines show bond formation and dotted lines show bond cleavage.
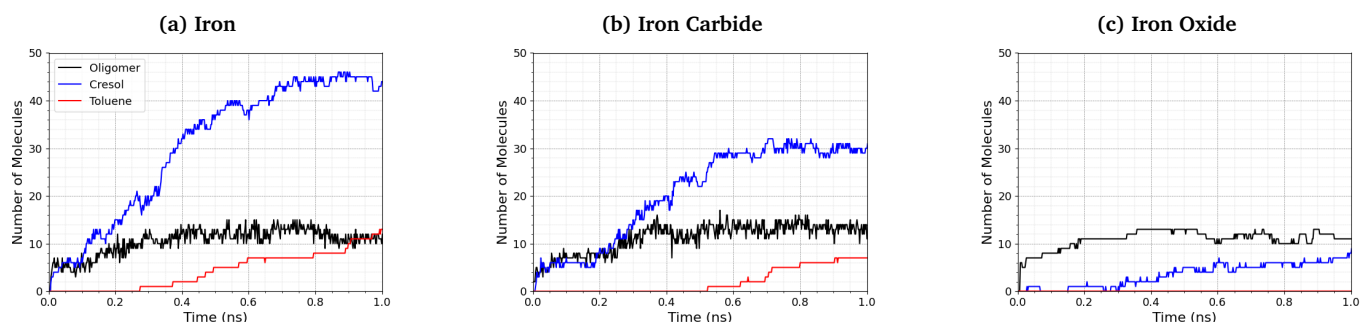

Fig. 8 Comparison of oligomer, toluene, and cresol quantities at 500 K and 3 GPa for the a) α-Fe(110), b) Fe$_3$C(010), and c) Fe$_3$O$_4$(001) systems.

pentamers, form in some cases. In general, longer polyphosphate chains are formed on the α-Fe(110) surfaces than Fe$_3$C(010) and particularly Fe$_3$O$_4$(001) surfaces. For α-Fe(110), a similar number of dimers and trimers form, with some of the chains growing up to octamers. The relatively short polyphosphate chains formed in our NEMD simulations are consistent with the average chain length of approximately 2.5 monomers found in tribometer experiments with ZDDP.[92] Much longer chains (up to 40 linked monomers) were formed in previous NEMD simulations with ReaxFF of phosphoric acid confined between sliding silica surfaces at very high temperature (1400 K).[93] The longer chains formed in these previous simulations is probably due to the higher reactivity of phosphoric acid compared to TCP and the lack of iron atoms to catalyse the depolymerisation (P-O dissociation) reactions.

The difference in the polyphosphate chain length between the three surfaces is much more subtle than the difference in TCP decomposition rates. This is probably because iron atoms or ions, which are most readily available in α-Fe(110), accelerate the depolymerisation of the polyphosphate chains by P-O bond cleavage.[92] Similarly, the polyphosphate chain length does not vary significantly over the wide range of temperatures and pressures studied in the NEMD simulations, as shown in the ESI (Figure S5). This is because both the polymerisation (P-O formation) and depolymerisation (P-O dissociation) reactions are accelerated by a similar amount due to increased temperature and shear stress, as shown in Figure 7.

3.6 Rate Analysis

Figure 10 shows the dependence of the TCP decomposition rate on shear stress for iron, iron carbide, and iron oxide surfaces. The decomposition rates were determined from the exponential decay fits shown in Figure 4 and the shear stress values were taken from Figure 3. The TCP decomposition rate increases exponentially with shear stress and also with temperature, suggesting that these reactions are stress-augmented thermally activated (SATA) processes.[94] The Bell model[95] can be used to describe the kinetics of SATA processes, and the rate constant, k, can be calculated as:

$$k = A \exp\left(-\frac{E_a - \tau \Delta V^*}{k_B T}\right) \quad (1)$$

where A is the pre-exponential factor, E_a is the activation energy, ΔV^* is the activation volume, and k_B is the Boltzmann constant. ΔV^* is sometimes interpreted as the difference in molecular volume between the transition state and the initial equilibrium state of the reactant.[96] A positive ΔV^* indicates that the volume of the transition state is larger (bond breaking), whereas a negative ΔV^* indicates the volume of the transition state is smaller (bond formation).[97] We use shear stress, τ, in the equation rather than normal stress, σ, due to experimental evidence that tribofilm growth is controlled by shear stress rather than normal stress.[9,10,97] While τ and σ are proportional (Figure 3), using σ results in smaller activation volumes by a factor of μ. For first-order reactions, as is the case here, the reaction rate, $r = k[C]$,
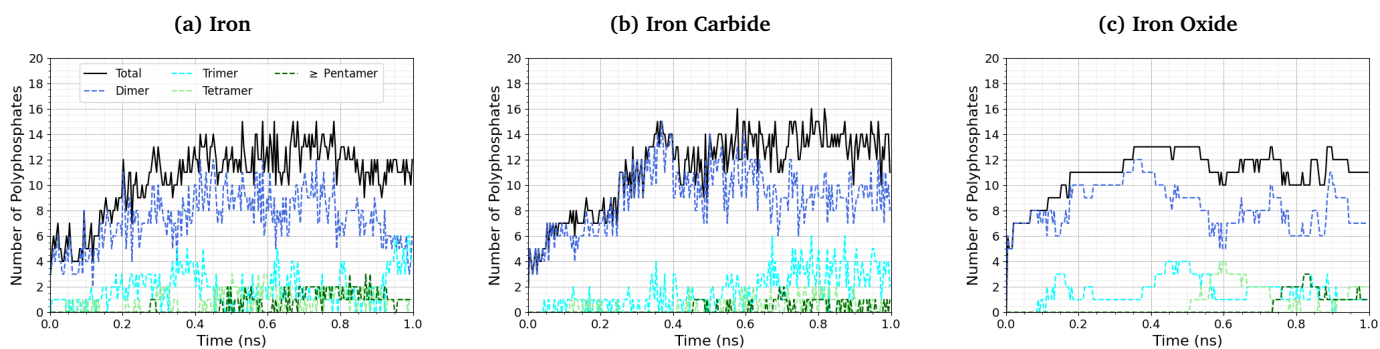
Fig. 9 Change in the number of polyphosphate chains with sliding time at 500 K and 3 GPa for a) α-Fe(110), b) Fe$_3$C(010) and c) Fe$_3$O$_4$(100) systems.
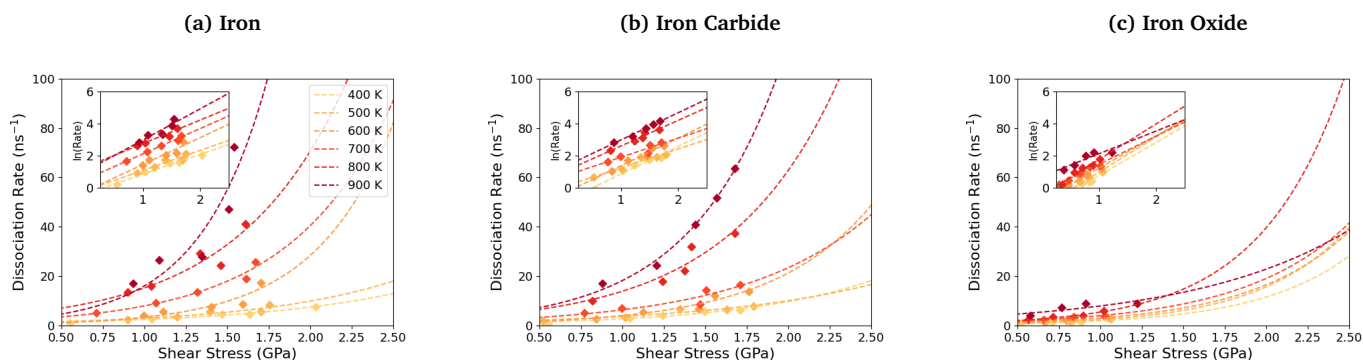

Fig. 10 Shear stress dependence of the TCP decomposition rate at different temperatures for a) α-Fe(110), b) Fe$_3$C(010), and c) Fe$_3$O$_4$(100) systems. Insets show the same data with a logarithmic y-axis.

where k is the rate constant and $[C]$ is the concentration of reactant. The Bell model[95] accurately describes the rate of TCP decomposition with temperature and shear stress on the three surfaces, as shown in the ESI (Figure S6).

The activation volume, ΔV^*, is calculated from the 2D fits of the rate versus shear stress data to Equation 1 shown in the insets of Figure 10. With this fitting method, ΔV^* is found to increase monotonically with temperature from 4.9 ± 1.7 Å^3 at 400 K to 17.5 ± 8.4 Å^3 at 900 K for TCP between the α-Fe(110) surfaces. For the Fe$_3$C(010) surfaces, ΔV^* also increases with temperature from 6.6 ± 3.7 Å^3 400 K to 15.3 ± 2.4 Å^3 at 900 K. For the Fe$_3$O$_4$(100) surfaces, ΔV^* increases from 8.3 ± 4.5 Å^3 at 400 K to 12.8 ± 6.6 Å^3 at 900 K. Thus, the calculated ΔV^* values are consistent with the dimensions of single bonds. The molecular volume of TCP is approximately 500 Å^3, meaning that the activation volumes for TCP on the three surfaces are between 1 and 4 % of the molecular volume. This percentage range is is consistent with previous NEMD simulations using trialkyl phosphates (4 %),[48] while experiments using ZDDPs with different alkyl substituent showed larger percentages (7-17 %).[57]

Based on the 2D fits to Equation 1 shown in Figure 10, the activation volume is highly temperature-dependant, but there is no clear trend between the three surfaces due to the relatively large uncertainties. Previous experimental studies of mechanochemical tribofilm growth have treated the activation volume as a

temperature-independent reaction constant; however, these studies considered a much smaller temperature range than the present study.[8–10,57,97] In our recent NEMD study of trialkyl phophate mechanochemical decomposition, we also observed that the the activation volume increased with increasing temperature.[48] This was partially explained through a reduction in the elastic modulus of the α-Fe(110) slabs. A recent DFT study suggested that the contribution of the elastic deformation of the surrounding bulk to the activation volume of mechanochemical reactions can be significant and, in some cases, dominant.[81] The elastic modulus of all three surfaces decreases with increasing temperature (Table S1). Since the activation volume is inversely proportional to the contact stiffness,[81] it is expected that higher temperatures will lead to lower activation energies, as observed in Figure 10 and Table S4. However, the increase in the activation volume (up to 350 %) is much larger than the decrease in the stiffness of the surfaces (up to 10 %) between 400-900 K. Thus, other factors, such as a decrease in stiffness of the TCP molecules and degradation products, must also contribute to the increased activation volume at higher temperature.

The activation energy, E_a, is calculated from the slope of the 2D fits of Equation 1 to the rate versus inverse temperature data shown in the ESI (Figure S7). For TCP decomposition between the α-Fe(110) surfaces, E_a increases with pressure from 20.6 ± 5.5 kJ mol^1 at 1 GPa to 24.0 ± 6.5 kJ mol^{-1} at 5 GPa. For the
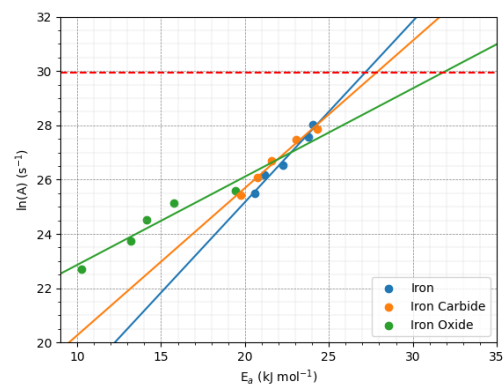
Fig. 11 Kinetic compensation effect between the activation energy and pre-exponential factor for Iron, Iron Carbide, and Iron Oxide

Fe$_3$C(010) surfaces, E_a also increases from 19.7 ± 6.1 kJ mol^{-1} at 1 GPa to 24.3 ± 7.5 kJ mol^{-1} at 5 GPa. For the Fe$_3$O$_4$(100) surfaces, E_a again increases from 10.2 ± 7.2 kJ mol^{-1} at 1 GPa to 19.5 ± 3.63 kJ mol^{-1} at 5 GPa. A previous experimental study suggested that the thermal activation energy for TCP decomposition on stainless steel is approximately 60 kJ mol^{-1}.[47] Thus, the activation energy values are considerably underpredicted in our simulations compared to experiments, which is probably due to the chromium-rich oxide layer formed on the surface of stainless steel in experiments,[98] which is known to be much less reactive towards TCP than iron oxides[33,34,99] as used in our NEMD simulations. Thus, the chromium oxide surface formed on stainless steel is expected to reduce the activation energy by a smaller amount than the iron oxides formed on conventional bearing steel.

The pre-exponential factor, A, is calculated from the intercept of the fits of Equation 1 to the rate versus inverse temperature data shown in the ESI (Figure S7). This is often expressed as $A = Z\rho$, where Z is the frequency or collision factor, and ρ is the steric factor. The steric factor represents the fraction of successful collisions and is usually less than unity.[100] For TCP molecules between the α-Fe(110) surfaces, $\ln(A)$ increases with pressure from 25.4 ± 3.2 at 1 GPa and to 28.1 ± 3.86 at 5 GPa. For the Fe$_3$C(010) surfaces, ln(A) increases from 25.4 ± 3.6 at 1 GPa to 27.8 ± 4.7 at 5 GPa, while it increases from 22.6 ± 4.5 to 25.6 ± 2.1 for the Fe$_3$O$_4$(100) surfaces. The low-pressure values are in good agreement with previous estimates of the pre-exponential factor for the thermal decomposition of TCP on stainless steel at atmospheric pressure, $\ln(A) = 22.7$.[47]

Figure 11 shows the variation of $\ln(A)$ with E_a from the 2D fits to the rate versus temperature data. The concurrent increase in E_a with $\ln(A)$, which is known as the kinetic compensation effect, is often observed in heterogeneously catalysed processes.[87] Previous studies using ReaxFF to study the mechanochemical behaviours of trialkyl phosphates have also observed such an effect.[48] The presence of a compensation effect suggests that the changes in these parameters may have a mathematical rather than physical origin and does not necessarily indicate any changes to the reaction pathway.[101]

Transition state theory[102] predicts a pre-exponential factor of about 10^{13} s^{-1} for first-order reactions, while experimental pre-exponential factors for surface reactions vary from 10^{10}-10^{16} s^{-1}.[103] Some previous mechanochemistry studies have used a constant pre-exponential factor of 10^{13} s^{-1} to determine the activation energy. If a constant pre-exponential factor of 10^{13} s^{-1} ($\ln(A) = 30$) is used for all three surfaces (horizontal red dashed line in Figure 11,[8] the activation energies of TCP decomposition for the three surfaces from the 2D fits increase in the order α-Fe(110) ~ Fe$_3$C(010) < Fe$_3$O$_4$(001). Thus, the more reactive surfaces towards TCP give lower activation energies, which is consistent with previous experiments of α-pinene tribopolymerisation.[18]

3.7 3D Fits

Surface	E_a (kJ mol^{-1})	$\ln(A)$ (s^{-1})	ΔV^* (Å^3)
α-Fe(110)	21.3±2.8	27.0±2.0	12.3±3.3
Fe$_3$C(010)	22.1±2.6	26.2±1.7	10.2±2.6
Fe$_3$O$_4$(100)	11.2±1.7	24.3±1.8	8.1±4.4

Table 1 Calculated values of the activation energy, E_a, natural logarithm of the pre-exponential factor, $\ln(A)$, and activation volume, ΔV^*, for TCP between α-Fe(110), Fe$_3$C(010) and Fe$_3$O$_4$(100) surfaces from the 3D fits to Equation 1. The parameter ranges represent the 95 % confidence intervals from the 3D fits.

To investigate the combined influence of temperature and stress on reactivity, the decomposition rate data was also plotted as a 3D surface and fitted to Equation 1. This approach provided significantly reduced uncertainties in the activation volume, activation energy, and pre-exponential factor compared to 2D fits in our previous NEMD study of trialkyl phosphate mechanochemistry.[48] To avoid biasing the 3D fits towards the higher decomposition rates, fits to the logarithm of the rate were employed.[48] The 3D fits for α-Fe(110), Fe$_3$C(010) and Fe$_3$O$_4$(100) are presented in Figures 12a), b), and c), respectively. Using the 3D surfaces, we calculated ΔV^*, E_a, and A values across the entire range of temperatures and pressures studied, as shown in Table 1. Unlike the 2D plots, the 3D fitting method did not capture the changes in the parameters with temperature and pressure. However, compared to the 2D fits, the 3D fits led to reduced uncertainties in all three parameters in the Bell model,[48] as shown in the ESI (Figures S8, S9, and S10). The 3D fits suggest that the activation energy increases in the order: Fe$_3$O$_4$(100) < Fe$_3$C(010) ~ α-Fe(110), which is opposite to that expected from the relative reactivity of the surfaces. The smaller energy barrier for the less reactive oxide surfaces may be due to the availability of oxygen atoms to promote P-O dissociation through nucleophilic substitution reactions at the phosphorus atoms. On the other hand, the pre-exponential factor is also much smaller for the iron oxide surface, suggesting that the fraction of successful collisions is also much lower. This may be due to the decreased availability of iron atoms at the surface, which are essential to promoting the dissociation reactions. Moreover, the ΔV^* values increase in the order: Fe$_3$O$_4$(100) < Fe$_3$C(010) < α-Fe(110), suggesting that the more reactive surfaces lead to an increased shear stress
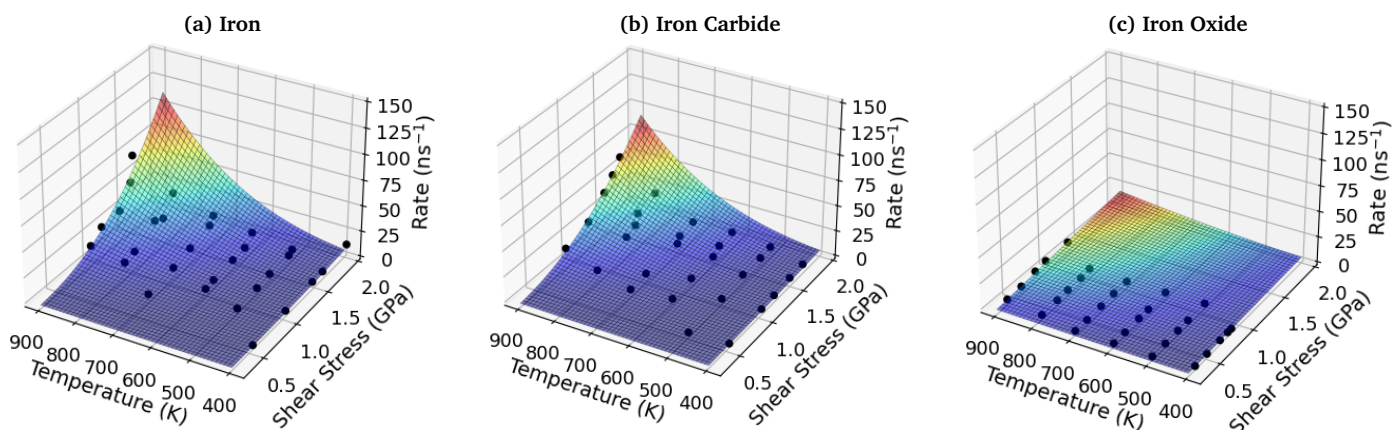
Fig. 12 3D fits of TCP decomposition rate as a function of temperature and shear stress for a) α-Fe(110), b) Fe$_3$C(010) and c) Fe$_3$O$_4$(100) surfaces.

dependence of the reactivity. The larger activation volume for α-Fe(110) than Fe$_3$C(010) and particularly Fe$_3$O$_4$(100) could be because the more reactive surfaces anchor the TCP molecules, leading to more efficient transmission of stress from the surfaces to the molecules, as suggested from previous NEMD simulations of different systems.[20,21] This observation contrasts with previous experiments α-pinene tribopolymerisation on a range of surfaces, which showed that surfaces that promoted α-pinene chemisorption (e.g. copper oxide) gave a smaller activation volume for the mechanochemical reaction than the ones only capable of physisorption (e.g. silicon oxide).[18] Another factor contributing to the difference in activation volumes between the three surfaces could be the contact stiffness.[48,81] In our NEMD simulations, at a given temperature, the stiffness of the three surfaces is quite similar (within 10 %), as shown in the ESI (Table S1). At most temperatures, the contact stiffness increases in the order Fe$_3$C(010) $< \alpha$-Fe(110) $<$ Fe$_3$O$_4$(100). Since the activation volume is expected to be inversely proportional to the contact stiffness,[81] the increased stiffness of the Fe$_3$O$_4$(100) surface may also contribute to its smaller activation volume compared to the other two surfaces. However, the differences in contact stiffness probably play a secondary role compared to the adsorption strength in determining the variation in activation volume between the three surfaces.

4 Conclusions

We have studied the mechanochemical decomposition of TCP molecules confined between atomically-smooth iron, iron carbide, and iron oxide surfaces using NEMD simulations with ReaxFF. The iron surfaces are more effective in promoting TCP decomposition compared to iron carbide and particularly iron oxide surfaces, which correlates with the increase in Fe-C bonding between the molecules and the surface, as well as the surface energy. The decomposition of TCP initially proceeds through P-O bond dissociation for all of the surfaces to form cresol molecules. In some cases, a subsequent C-O bond dissociation in the cresol molecule led to the formation of toluene. We also investigate the early stages of polyphosphate tribofilm growth. Despite the fact that P-O bond formation is accelerated on the more reac-

tive surfaces, the rate of P-O bond cleavage is also increased by a similar amount, meaning that the total number of P-O bonds is comparable between the three surfaces. The polyphosphate chain length is also similar between the surfaces, with a skew in the distribution to higher chain lengths (up to octomers) for the more reactive iron surfaces. The rate of TCP decomposition increases exponentially with temperature and shear stress, indicating that this is a SATA process. 3D fits to the Bell model lead to activation energies and pre-exponential factors both increasing in the order: Fe$_3$O$_4$(100) $<$ Fe$_3$C(010) $\sim \alpha$-Fe(110). This implies that, although the energy barrier is smaller for the less reactive oxide surfaces, the fraction of successful collisions is also much lower. This trend may be due to the decreased availability of iron atoms on the surface, which are essential to promoting the decomposition reactions. The activation volume increases in the order: Fe$_3$O$_4$(100) $<$ Fe$_3$C(010) $< \alpha$-Fe(110), which suggests that higher surface energy causes the TCP molecules to be anchored to the surface, leading to more efficient transmission of shear stress. An additional contribution to the larger activation energy for α-Fe(110) surfaces could be the reduced contact stiffness. We have shown that surface chemistry plays a central role in the mechanochemical decomposition of an industrially important lubricant additive. The differences between the three ferrous surfaces can be rationalised through parameters from the Bell model. Future simulations could consider the impact of heterogeneous surfaces, such as steel on mechanochemical reactions. Experiments could consider using more controllable surfaces, such as specific iron oxides, for optimal comparison with molecular simulations of nanoscale contacts.

Author Contributions

We strongly encourage authors to include author contributions and recommend using CRediT for standardised contribution descriptions. Please refer to our general author guidelines for more information about authorship.

Conflicts of interest

There are no conflicts to declare.

Acknowledgements

References

1   R. T. O'Neill and R. Boulatov, *Nature Reviews Chemistry*, 2021, **5**, 148–167.

2   E. Colacino, M. Carta, G. Pia, A. Porcheddu, P. C. Ricci and F. Delogu, *ACS Omega*, 2018, **3**, 9196–9209.

3   S. L. James, C. J. Adams, C. Bolm, D. Braga, P. Collier, W. Jones, A. Krebs, J. Mack, L. Maini, A. G. Orpen, I. P. Parkin, W. C. Shearouse, W. Steed and D. C. Waddell, *Chemical Society Reviews*, 2012, **41**, 413–447.

4   A. A. Michalchuk, I. A. Tumanov and E. V. Boldyreva, *CrystEngComm*, 2019, **21**, 2174–2179.

5   R. A. Haley, A. R. Zellner, J. A. Krause, H. Guan and J. Mack, *ACS Sustainable Chemistry and Engineering*, 2016, **4**, 2464–2469.

6   S. Hwang, S. Grätz and L. Borchardt, *Chemical Communications*, 2022, **58**, 1661–1671.

7   A. Boscoboinik, D. Olson, H. Adams, N. Hopper and W. T. Tysoe, *Chemical Communications*, 2020, **56**, 7730–7733.

8   N. N. Gosvami, J. A. Bares, F. Mangolini, A. R. Konicek, D. G. Yablon and R. W. Carpick, *Science*, 2015, **348**, 102–106.

9   J. Zhang and H. Spikes, *Tribology Letters*, 2016, **63**, 24.

10 J. Zhang, J. P. Ewen, M. Ueda, J. S. Wong and H. A. Spikes, *ACS Applied Materials & Interfaces*, 2020, **12**, 6662–6676.

11 A. Neville, A. Morina, T. Haque and M. Voong, *Tribology International*, 2007, **40**, 1680–1695.

12 P. Mittal, Y. Maithani, J. P. Singh and N. N. Gosvami, *Tribology International*, 2020, **151**, 106419.

13 C. McFadden, C. Soto and N. D. Spencer, *Tribology International*, 1997, **30**, 881–888.

14 M. Ueda, A. Kadiric and H. Spikes, *Tribology Online*, 2020, **15**, 318–331.

15 M. Ueda, A. Kadiric and H. Spikes, *Tribology Letters*, 2021, **69**, 62.

16 S. Peeters, A. Barlini, J. Jain, N. N. Gosvami and M. C. Righi, *Applied Surface Science*, 2022, **600**, 153947.

17 V. R. S. Ruiz, T. Kuwahara, J. Galipaud, K. Masenelli-Varlot, M. B. Hassine, C. Héau, M. Stoll, L. Mayrhofer, G. Moras, J. M. Martin, M. Moseler and M.-I. de Barros Bouchet, *Nature Communications*, 2021, **12**, 4550.

18 X. He and S. H. Kim, *Langmuir*, 2018, **34**, 2432–2440.

19 A. Khajeh, X. He, J. Yeon, S. H. Kim and A. Martini, *Langmuir*, 2018, **34**, 5971–5977.

20 J. Yeon, X. He, A. Martini and S. H. Kim, *ACS Applied Materials & Interfaces*, 2017, **9**, 3142–3148.

21 T. Kuwahara, P. A. Romero, S. Makowski, V. Weihnacht, G. Moras and M. Moseler, *Nature Communications*, 2019, **10**, 151.

22 B. Guan, B. A. Pochopien and D. S. Wright, *Lubrication Science*, 2016, **28**, 257–265.

23 D. W. Johnson and J. E. Hils, *Lubricants*, 2013, **1**, 132–148.

24 O. Beeck, J. Givens and E. Williams, *Proceedings of the Royal Society of London, Series A*, 1940, **177**, 103–118.

25 D. H. Han and M. Masuko, *Tribology Transactions*, 1999, **42**, 902–906.

26 J. Airey, J. Simpson, M. Spencer, R. W. Greenwood and M. J. Simmons, *Proceedings of the Institution of Mechanical Engineers, Part J*, 2023, **237**, 1548–1567.

27 R. L. Jones, H. Ravner and R. L. Cottington, *ASLE Transactions*, 1970, **13**, 1–10.

28 F. Barcroft and S. Daniel, *Journal of Basic Engineering*, 1965, **87**, 761–767.

29 D. Godfrey, *ASLE Transactions*, 1965, **8**, 1–11.

30 O. D. Faut and D. R. Wheeler, *ASLE Transactions*, 1983, **26**, 344–350.

31 A. H. J. M. Gauthier, H. Montes and J. M. Georges, *ASLE Transactions*, 1982, **25**, 445–455.

32 C. Saba and N. Forster, *Tribology Letters*, 2002, **12**, 135–146.

33 D. W. Johnson, S. Morrow, N. H. Forster and C. S. Saba, *Chemistry of Materials*, 2002, **14**, 3767–3775.

34 B. Acharya, T. Pardue, K. Avva and J. Krim, *Tribology International*, 2018, **126**, 106–115.

35 J. F. Luiz and H. Spikes, *Tribology Letters*, 2020, **68**, 75.

36 H. Spikes, *Tribology Letters*, 2004, **17**, 469–489.

37 D. R. Wheeler and O. D. Faut, *Applications of Surface Science*, 1984, **18**, 106–122.

38 D. Sung and A. Gellman, *Tribology International*, 2002, **35**, 579–590.

39 R. D. Evans, K. L. More, C. V. Darragh and H. P. Nixon, *Tribology Transactions*, 2004, **47**, 430–439.

40 R. D. Evans, K. L. More, C. V. Darragh and H. P. Nixon, *Tribology Transactions*, 2005, **48**, 299–307.

41 A. Khajeh, F. H. Bhuiyan, J.-E. Mogonye, R. A. Pesce-Rodriguez, S. Berkebile and A. Martini, *The Journal of Physical Chemistry C*, 2021, **125**, 5076–5087.

42 H. K. D. H. Bhadeshia, *Progress in Materials Science*, 2012, **57**, 268–435.

43 D. W. Johnson, J. E. Hils and N. Forster, *Tribology Letters*, 2011, **42**, 223–232.

44 A. Stukowski, *Modelling and Simulation in Materials Science and Engineering*, 2009, **18**, 015012.

45 A. Khajeh, X. Hu, K. Mohammadtabar, Y. K. Shin, A. C. Van Duin, S. Berkebile and A. Martini, *The Journal of Physi-*

cal Chemistry C, 2019, **123**, 12886–12893.

46 J. P. Ewen, C. A. Latorre, C. Gattinoni, A. Khajeh, J. D. Moore, J. E. Remias, A. Martini and D. Dini, *The Journal of Physical Chemistry C*, 2020, **124**, 9852–9865.

47 J. F. Makki and E. E. Graham, *Tribology Transactions*, 1990, **33**, 595–603.

48 C. Ayestarán Latorre, J. E. Remias, J. D. Moore, H. A. Spikes, D. Dini and J. P. Ewen, *Communications Chemistry*, 2021, **4**, 178.

49 J. P. Ewen, D. M. Heyes and D. Dini, *Friction*, 2018, **6**, 349–386.

50 C. Winder and J. C. Balouet, *Environmental Research*, 2002, **89**, 146–164.

51 R. Lu, K. Kobayashi, H. Nanao and S. Mori, *Tribology Letters*, 2009, **33**, 1–8.

52 E. E. Klaus, J. Phillips, S. C. Lin, N. L. Wu and J. L. Duda, *Tribology Transactions*, 1990, **33**, 25–32.

53 P. Blonski and A. Kiejna, *Surface Science*, 2007, **601**, 123–133.

54 W. C. Chiou and E. A. Carter, *Surface Science*, 2003, **530**, 88–100.

55 R. Bliem, E. McDermott, P. Ferstl, M. Setvin, O. Gamba, J. Pavelec, M. A. Schneider, M. Schmid, U. Diebold, P. Blaha, L. Hammer and G. S. Parkinson, *Science.*, 2014, **346**, 1215–1218.

56 K. Mohammadtabar, S. J. Eder, N. Dörr and A. Martini, *Tribology International*, 2022, **176**, 107922.

57 J. Zhang, J. P. Ewen and H. A. Spikes, *Molecular Systems Design & Engineering*, 2022, **7**, 1045–1055.

58 A. P. Thompson, H. M. Aktulga, R. Berger, D. S. Bolintineanu, W. M. Brown, P. S. Crozier, P. J. in't Veld, A. Kohlmeyer, S. G. Moore, T. D. Nguyen *et al.*, *Computer Physics Communications*, 2022, **271**, 108171.

59 L. Verlet, *Physical Review*, 1967, **159**, 98.

60 T. Schneider and E. Stoll, *Physical Review B*, 1978, **17**, 1302–1322.

61 X. Yong and L. T. Zhang, *The Journal of Chemical Physics*, 2013, **138**, 084503.

62 K. Mohammadtabar, S. J. Eder, N. Dörr and A. Martini, *The Journal of Physical Chemistry C*, 2019, **123**, 19688–19692.

63 F. H. Bhuiyan, S. H. Kim and A. Martini, *Applied Surface Science*, 2022, **591**, 153209.

64 M. Koyama, J. Hayakawa, T. Onodera, K. Ito, H. Tsuboi, A. Endou, M. Kubo, C. A. D. Carpio and A. Miyamoto, *Journal of Physical Chemistry B*, 2006, **110**, 17507–17511.

65 S. Loehlé and M. Righi, *Lubricants*, 2018, **6**, 31.

66 S. J. Plimpton and A. P. Thompson, *MRS Bulletin*, 2012, **37**, 513–521.

67 A. C. Van Duin, S. Dasgupta, F. Lorant and W. A. Goddard, *The Journal of Physical Chemistry A*, 2001, **105**, 9396–9409.

68 T. P. Senftle, S. Hong, M. M. Islam, S. B. Kylasa, Y. Zheng, Y. K. Shin, C. Junkermeier, R. Engel-Herbert, M. J. Janik, H. M. Aktulga *et al.*, *npj Computational Materials*, 2016, **2**, 1–14.

69 A. Martini, S. J. Eder and N. Dörr, *Lubricants*, 2020, **8**, 44.

70 A. K. Rappe and W. A. Goddard III, *The Journal of Physical Chemistry*, 1991, **95**, 3358–3363.

71 M. Aryanpour, A. C. van Duin and J. D. Kubicki, *The Journal of Physical Chemistry A*, 2010, **114**, 6298–6307.

72 C. Zou, A. C. Van Duin and D. C. Sorescu, *Topics in Catalysis*, 2012, **55**, 391–401.

73 C. Verlackt, E. Neyts, T. Jacob, D. Fantauzzi, M. Golkaram, Y. K. Shin, A. Van Duin and A. Bogaerts, *New Journal of Physics*, 2015, **17**, 103005.

74 K. Chenoweth, A. C. V. Duin and W. A. Goddard, *Journal of Physical Chemistry A*, 2008, **112**, 1040–1053.

75 L. S. Morrissey, S. M. Handrigan, S. Subedi and S. Nakhla, *Molecular Simulation*, 2019, **45**, 501–508.

76 J. J. Adams, D. Agosta, R. Leisure and H. Ledbetter, *Journal of Applied Physics*, 2006, **100**, 113530.

77 J. Li, H. K. Mao, Y. Fei, E. Gregoryanz, M. Eremets and C. S. Zha, *Physics and Chemistry of Minerals*, 2002, **29**, 166–169.

78 H. J. Reichmann and S. D. Jacobsen, *American Mineralogist*, 2004, **89**, 1061–1066.

79 M. M. Islam, C. Zou, A. C. V. Duin and S. Raman, *Physical Chemistry Chemical Physics*, 2015, **18**, 761–771.

80 T. D. Ta, H. M. Le, A. K. Tieu, H. Zhu, H. T. T. Ta, N. V. Tran, S. Wan and A. C. T. van Duin, *ACS Applied Nano Materials*, 2020, **3**, 2687–2704.

81 Z. Li and I. Szlufarska, *Physical Review Letters*, 2021, **126**, 076001.

82 G. Clavier, N. Desbiens, E. Bourasseau, V. Lachet, N. Brusselle-Dupend and B. Rousseau, *Molecular Simulation*, 2017, **43**, 1413–1422.

83 K. Sebeck, C. Shao and J. Kieffer, *ACS Applied Materials and Interfaces*, 2016, **8**, 16885–16896.

84 J. P. Gao, W. D. Luedtke, D. Gourdon, M. Ruths, J. N. Israelachvili and U. Landman, *The Journal of Physical Chemistry B*, 2004, **108**, 3410–3425.

85 X. Yu, C. F. Huo, Y. W. Li, J. Wang and H. Jiao, *Surface Science*, 2012, **606**, 872–879.

86 X. Chen, K. Kawai, H. Zhang, K. Fukuzawa, N. Koga, S. Itoh and N. Azuma, *The Journal of Physical Chemistry C*, 2020, **124**, 22496–22505.

87 E. Roduner, *Chemical Society Reviews*, 2014, **43**, 8226–8239.

88 S. S. Tafreshi, A. Roldan, N. Y. Dzade and N. H. De Leeuw, *Surface Science*, 2014, **622**, 1–8.

89 E. Osei-Agyemang, S. Berkebile and A. Martini, *Tribology Letters*, 2018, **66**, 1–22.

90 B. Jiang, M. Yang, D. Xie and H. Guo, *Chemical Society Reviews*, 2016, **45**, 3621–3640.

91 S. Peeters, C. Charrin, I. Duron, S. Loehlé, B. Thiebaut and M. C. Righi, *Materials Today Chemistry*, 2021, **21**, 100487.

92 R. Heuberger, A. Rossi and N. D. Spencer, *Tribology Letters*, 2007, **25**, 185–196.

93 D. C. Yue, T. B. Ma, Y. Z. Hu, J. Yeon, A. C. V. Duin, H. Wang and J. Luo, *Journal of Physical Chemistry C*, 2013, **117**,

25604–25614.

94 H. Spikes, *Friction*, 2018, **6**, 1–31.

95 G. I. Bell, *Science*, 1978, **200**, 618–627.

96 B. Chen, R. Hoffmann and R. Cammi, *Angewandte Chemie International Edition*, 2017, **56**, 11126–11142.

97 L. Fang, S. Korres, W. A. Lamberti, M. N. Webster and R. W. Carpick, *Faraday Discussions*, 2023, **241**, 394–412.

98 C. A. Olsson and D. Landolt, *Electrochimica Acta*, 2003, **48**, 1093–1104.

99 M. Abdelmaksoud, J. W. Bender and J. Krim, *Tribology Letters*, 2002, **13**, 179–186.

100 M. G. Evans and M. Polanyi, *Transactions of the Faraday Society*, 1935, **31**, 875–894.

101 P. J. Barrie, *Physical Chemistry Chemical Physics*, 2012, **14**, 318–326.

102 D. G. Truhlar, W. L. Hase and J. T. Hynes, *The Journal of Physical Chemistry*, 1983, **87**, 2664–2682.

103 H. Lynggaard, A. Andreasen, C. Stegelmann and P. Stoltze, *Progress in Surface Science*, 2004, **77**, 71–137.